Aerodynamical behavior of spherical debris in the supersonic and rarefied wind tunnel MARHy

Viviana Lago, Nicolas Rembaut, Romain Joussot

Aerodynamical behavior of spherical debris in the supersonic and rarefied wind tunnel MARHy*

Nicolas Rembaut[1,*], Romain Joussot[1], Viviana Lago[1]

1c av. de la Recherche Scientifique, CS 50060, F-45071, Orléans cedex 2, France.

Abstract

The atmospheric re-entry of space debris poses a significant risk to humans in the event of a ground impact. Predicting the trajectory of space debris is still a very complex task. The debris passes through different flow regimes and this makes it difficult to correctly estimate its aerodynamic behavior. This work responds to the need of setting up experimental databases in the transition and the slip flow regimes that will enable to validate the numerical codes. This paper presents the experimental results based on the study of the influence of rarefied effects on the shock shapes around the spheres. The experiments were conducted in the MARHy super-hypersonic rarefied wind tunnel, with flows at Mach 4 and Knudsen numbers ranging from 3×10^{-3} to 6×10^{-2}. The shape of the shock waves and the standoff were determined by CMOS camera visualization. The total pressure flow field around the spheres was measured by a Pitot tube. Numerical modelling for a test case was performed using the Monte Carlo code DS2V, and validated with the experimental measurements.

Keywords: Experimental investigations, Space Debris, Supersonic rarefied flows, Slip flow regime

2020 MSC: 00-01, 99-00

*This document is an update of the research project presented at The First International Orbital Debris Conference (IOC), 9-12 December 2019 in Houston, Texas, title "Debris characterization in the super/hypersonic and rarefied wind tunnel MARHy".

*Corresponding author

Email address: nicolas.rembaut@cnrs-orleans.fr (Nicolas Rembaut)

[1]CNRS, ICARE, UPR 3021

1. Introduction

With the constant increase in the number of artificial satellites and the emergence of the satellite constellations and CubeSat, the frequency of re-entry debris on Earth will increase considerably in the future. Indeed, at the end of their activity, these non-stationary satellites or debris will slow down and leave its orbit, especially those in the low orbit due to the presence of atmospheric drag [1].

Most of the debris entering the atmosphere is too small to survive re-entry as it is entirely consumed in the upper atmosphere by melting and vaporization. Larger debris, especially debris made of high-melting materials such as titanium or stainless steel, may either survive partially or remain completely intact and reach the ground. If the spacecraft contains active or radioactive materials, it is extremely important to know where exactly these fragments fall on the Earth's surface. It is therefore, essential to be able to predict their trajectory to minimize the risk to the human population. Nevertheless, predicting the re-entry of space debris remains an open problem as it is a multi-physical task involving steady-state and rarefied aerodynamic simulations, heat transfer calculations and structural failure predictions [2].

For this purpose, several codes have been developed by different space agencies such as DAS (NASA), ORSAT (NASA) [3], ORSAT-J (JAXA), DRAMA/ SESAM (ESA) [4], DEBRISK (CNES) [5], DRAPS (China), SCARAB (ESA-HTG Germany)[6], PAMPERO (CNES) [7], FOSTRAD [8][9].

These 'Debris predictory codes' can be classified into two categories: object-oriented models and spacecraft-oriented models [10]. The first category uses predefined fragments and assumes a fixed decay altitude regardless of the re-entry flight history. Nevertheless, it is known that drag strongly depends on gas-surface interaction which changes with the orbital altitudes, conditioning the orbital decay of satellites and debris [11]. The second category is the spacecraft-oriented software which includes more complex models with an extensive database of material characteristics and is capable of predicting frag-

mentation events and patterns, as well as their aerodynamic behavior and heat flux [6].

However, there are many uncertainties affecting the ability to make accurate predictions such as object geometries, aerodynamic coefficients, material properties, unknown initial flight conditions or invalidated model parameters. Indeed, when an object enters the atmosphere it passes through different flow regimes, each of them is characterized by a decreasing degree of rarefaction: free molecular, transitional, slip and continuous regime. Powerful numerical simulations such as DSMC and CFD can be applied in the appropriate regime, but they can be very costly in terms of time consuming. To simplify these numerical simulations, codes which are less expensive in calculation time have been developed by using 'low fidelity' models. These models are built on the hypersonic local panel inclination method that are based on the modified Newtonian theory and have been developed to simulate among other the ablation of spacecraft entering the atmosphere. This approximation gives reasonable aerothermal results for hemispherical objects, but is less efficient for characterizing cubic or sharp-edged objects [12].

In addition, these models are only valid for hypersonic/supersonic flows in continuous regime. In case of free molecular regime, these low-fidelity models may provide reliable results when using analytical models, such as the Schaaf and Chamber flat plate model [13]. The task becomes more complicated to characterize the transition and slip flow regime as the method is based on generating bridging functions that could lead to large uncertainties [14]. It is easy to understand that physical parameters and models used to determine, 'in fine' point of impact on Earth of an initial object falling back from space at high-speed are tainted with uncertainties, and have to be verified and validated. Currently, there is a lack of experimental data to validate the simplified models and geometries used by these codes, particularly in rarefied flow regimes with viscous interaction properties that can modify shock shapes, aerodynamic coefficients, and surface/gas interactions.

The objective of this work is to provide experimental databases that could

be used to improve the physical aerodynamic models implemented to determine the survivability and trajectory of space debris. These debris, resulting from fragmentation, may have any shape that has never been studied aerodynamically under rarefied regime. Although, many debris found on the ground is spherical in shape [15].

The present work focuses on the experimental study of the aerodynamic properties of spherical debris in Mach 4 rarefied flows ranging from the transitional to the near continuous regime [16]. This experimental study was carried out in the MARHy hypersonic rarefied wind tunnel, belonging to the ICARE laboratory of the CNRS in Orléans, France. Three Mach 4 nozzles operating at different static pressures: 2.66, 7.99 and 71 Pa, were used to study the flow around the spheres of different diameters in order to experimentally cover a range of Knudsen numbers large enough to switch from near-continuous to slip regimes [17]. The shape of the shock wave was studied by glow discharge visualization and a pressure probe was used to measure the total pressure fields around the models. The shock wave shape and the standoff distance were determined for each test condition, and were compared to those predicted by the empirical Billig's equation. To complete this experimental study, a Monte Carlo numerical simulation with the code DS2V is presented in this work for test case of Mach $4 - 7.99$ Pa and 40 mm diameter sphere. The objective is to show the relevance of the accommodation coefficients which can be an important source of uncertainty in the calculation of rarefied flow aerodynamic properties around an object.

2. Experimental setup

This study was carried out in the MARHy (Hypersonic Rarefied Adaptable Mach) wind tunnel, one of the three facilities of the FAST platform: 'Facilities for Aerothermodynamics & Supersonic Technologies'. This platform consists of a set of three wind tunnels which can simulate experimentally the different re-entry phases conditions.

2.1. The MARHy wind tunnel

The MARHy facility, previously known as SR3 [18], is a rarefied supersonic/hypersonic continuous operating wind tunnel. A detailed layout of the wind tunnel is shown in Fig. 1. The MARHy wind tunnel consists of a main chamber and a pumping unit. The main chamber is an assembly of three parts. In the direction of flow, there is a settling chamber at the entrance. This large volume chamber serves as a gas reservoir for supersonic nozzles where the stagnation pressure is regulated by a micrometric valve. The nozzle is located at the interface of the settling chamber and the experimental chamber where the super/hypersonic flow will expand at low pressure and high speed. The experimental chamber is 5 m long and has a diameter of 2 m. This large size allows to avoid wall effects and also makes it easier to set up the experiments. The experimental chamber is coupled to a diffuser which is connected to the pumping unit to evacuate the gases and maintain low pressure during experiments. The pumping unit consists of 2 primary pumps, 2 intermediate vacuum Roots type-blowers and 12 high vacuum Roots type-blowers. This pumping unit provides the required vacuum level for the desired flow density conditions in continuous operation. Depending on the degree of rarefaction required, the number of Roots type-blowers used can be adjusted.

This facility is operated with a set of nozzles producing flow conditions from Mach 0.6 to Mach 30 [19]. The geometry of each nozzle has been shaped to provide an isentropic, laminar flow and perfectly homogeneous in its core. For each nozzle, the isentropic flow depends on the inlet temperature T_0 and pressure P_0, and on the pressure in the experiment chamber P_1. These three parameters are adjusted at the beginning of the experiment and remain constant throughout the duration of the tests. Due to the rarefaction effects, a thick or thin boundary layer develops along the divergent part of the nozzles giving a homogeneous core diameter smaller than the nozzle diameter. In order to obtain reliable results, the experimental models' sizes are adapted to the isentropic core diameter.

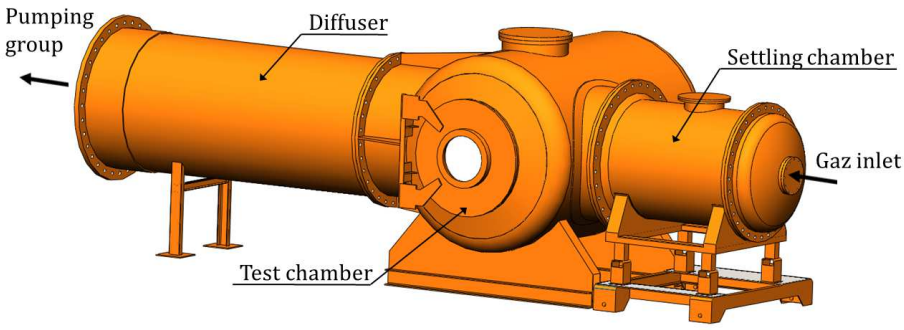

Figure 1: Scheme of the MARHy wind tunnel.

2.2. Experimental conditions and diagnostics

The purpose of this study is to determine the influence of rarefaction effects on the shock wave formed around a sphere. The degree of rarefaction will be characterized by the Knudsen number which is the dimensionless number described by the ratio of the mean free path to the characteristic size of the object, in the present case is the diameter of the spheres. The chosen experimental conditions allow to vary the Knudsen number from the continuous regime to the slip regime, with iso-Mach conditions, because a change in the flow Mach number could also modify the interaction with the object. Three nozzles were selected, all operating at Mach 4 but with different pressure conditions 71 Pa, 7.99 Pa and 2.66 Pa. The operating parameters of the nozzles are detailed in Tab. 1-3.

So as to have a wide range of Knudsen numbers, 5 different diameters of spheres were selected 5, 10, 25, 30 and 40 mm. In Fig. 2 the Knudsen number is ploted as a function of the radius of the spheres corresponding to our experimental conditions.

Stagnation conditions	Free stream conditions
$p_0 = 404$ Pa	$p_1 = 2.66$ Pa
$T_0 = 293$ K	$T_1 = 69.76$ K
$\rho_0 = 4.8 \times 10^{-3}$ kg.m^{-3}	$\rho_1 = 1.3 \times 10^{-4}$ kg.m^{-3}
	$\mu_1 = 4.77 \times 10^{-6}$ Pa.s
	$U_1 = 669.61$ m.s^{-1}
	$M_1 = 4$
	$\lambda_1 = 0.318$ mm
	$Re = 1866$

Table 1: N1 Operating conditions.

Stagnation conditions	Free stream conditions
$p_0 = 1214$ Pa	$p_1 = 7.99$ Pa
$T_0 = 293$ K	$T_1 = 69.76$ K
$\rho_0 = 1.44 \times 10^{-2}$ kg.m^{-3}	$\rho_1 = 3.99 \times 10^{-4}$ kg.m^{-3}
	$\mu_1 = 4.77 \times 10^{-6}$ Pa.s
	$U_1 = 670$ m.s^{-1}
	$M_1 = 4$
	$\lambda_1 = 0.106$ mm
	$Re = 5603$

Table 2: N2 Operating conditions.

Stagnation conditions	Free stream conditions
$p_0 = 10797$ Pa	$p_1 = 71$ Pa
$T_0 = 293$ K	$T_1 = 69.76$ K
$\rho_0 = 1.28 \times 10^{-3}$ kg.m^{-3}	$\rho_1 = 3.55 \times 10^{-3}$ kg.m^{-3}
	$\mu_1 = 4.77 \times 10^{-6}$ Pa.s
	$U_1 = 670$ m.s^{-1}
	$M_1 = 4$
	$\lambda_1 = 0.012$ mm
	$Re = 49818$

Table 3: N3 Operating conditions.

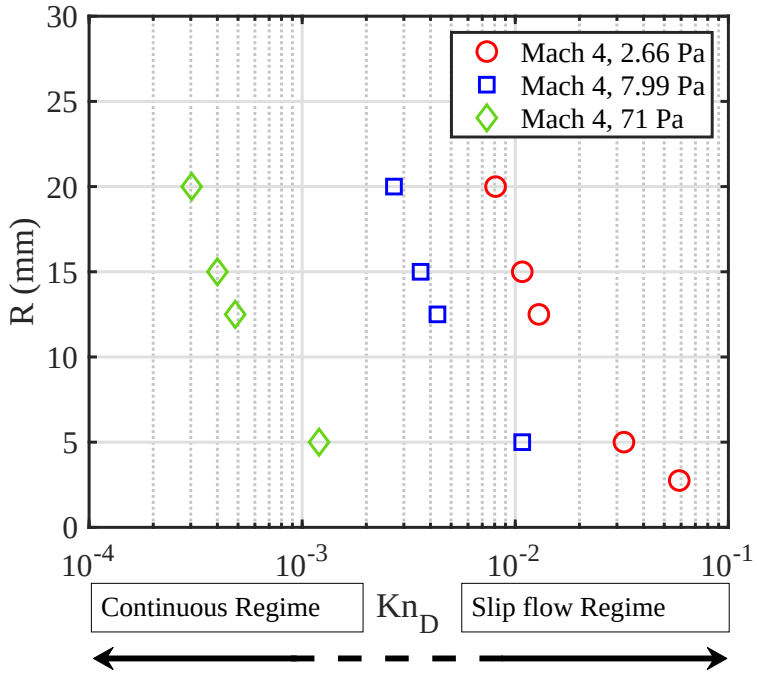

Figure 2: Flow conditions tested in terms of Knudsen numbers Kn_D and radius of sphere R.

2.3. Experimental set-up

The spheres are held with a shaped support profiled to minimize flow obstruction. They are aligned with the flow axis and placed at a distance of 7 cm from the nozzle outlet as shown in Fig. 4. To analyze the shock around the spheres, two diagnostic technics were used: the pitot probe and the luminescence visualization technique. These technics are complementary to each other and their feasibility depends on the operating conditions.

2.3.1. The stagnation pressure measurement

Total pressure of the flow field around the sphere is measured with a Pitot probe. The Pitot probe is a stainless steel tube with a flat-ended cylinder with an outer diameter of 2.3 mm and an inner diameter of 1.18 mm. Pressures are measured with absolute capacitance manometers (MKS, 600 series Baratron) whose full scale range were adapted to the pressure values of the experimental conditions: 0-100 torr for Mach 4, 71 Pa and 0-10 torr for Mach 4, 7.99 and 2.66 Pa. The manometers are connected to a MKS control unit (PR 4000B) with a 12-bit resolution. A 3-axis traversing system controlled by a computer ensures the displacement of the Pitot probe with a step resolution on each axis of 0.12 mm $\pm$ 0.02 mm on each position. Despite low pressure conditions, no orifice corrections due to viscous effects have to be applied to the pressure measurements probes [20][21].

2.3.2. The flow field visualization

Commonly techniques such as PIV or Schlieren used to visualize flow fields around models cannot be applied because of the low pressure operating conditions, especially for the N1 and N2 nozzles. In rarefied flows these techniques are replaced by the use of electron beam fluorescence [22] or the glow discharge technique which is used for this study. This technique consists of weakly ionizing the flow by applying a low voltage to a metallic electrode placed in the flow [23][24]. The variations in the light intensity show local variations in density,

thus making it possible to visualize the shock around obstacles, as shown in Fig. 5.

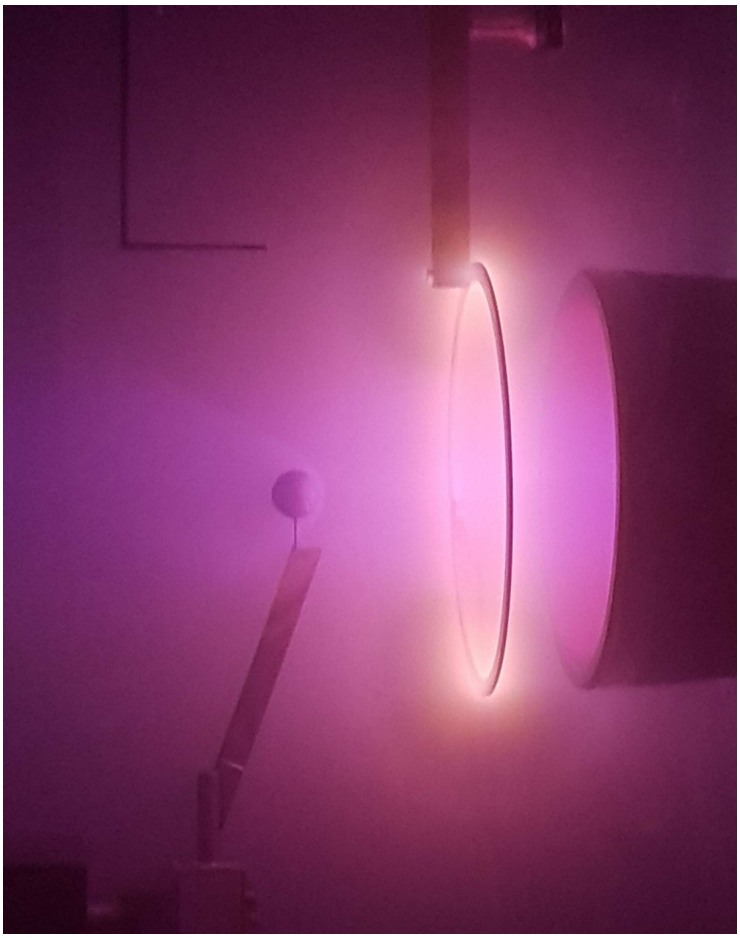

Figure 3: Picture of glow discharge visualization of the shock wave around a spherical body, at Mach 4 − 7.99 Pa.

For the present study, a copper ring electrode is placed at the nozzle outlet parallel to its plane to uniformly ionize the flow as shown in Fig. 4. The diameter of the ring is larger than the outlet diameter of the nozzle in order to avoid any disturbance to the flow. The bias voltages are between -1 and -2 kV, giving discharge currents of the order of 5 mA maximum, and powers of the order of 10 W maximum is insufficient to modify the nature of flows [17].

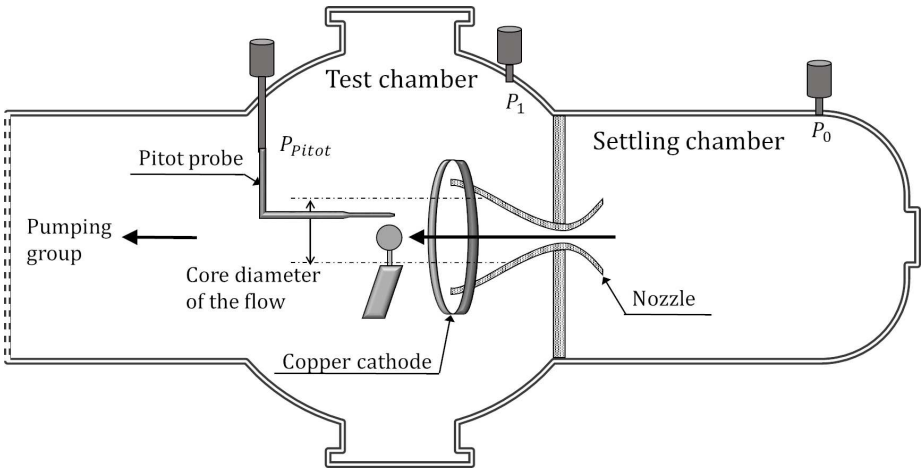

Figure 4: Schematic view of the experimental setup in the test chamber.

The diffuse light emitted by the flow field is focused through a CaF_2 window on the back-illuminated KURO-CMOS camera (2048 × 2048 array), equipped with a 94 mm, f/4.1 VUV objective lens. This optical configuration gives a spatial resolution of 6.25 pixels/mm. Spectral analysis of the light emitted by the glow discharge showed that the intensity is due to the emission of the N_2 2nd positive system $(C^3\pi_u \rightarrow B^3\pi_g)\Delta v = 0$ at 337 nm and the N_2^+ first negative system $(B^2\Sigma_u \rightarrow X^2\Sigma_u)\Delta v = 0$ at 390.14 nm [25][19]. This analysis showed that it is important to have an optical system with good performance in the VUV and near VUV spectral region in order to not degrade the spectral transmission bandwidth and to be able to apply mathematical methods based on the detection of the gradients to detect the shock with a good accuracy.

Results and discussion

In the transitional and the slip regime, there is no analytical formulation to describe the shock around the spheres. Nevertheless, shock wave shapes around a spherical body moving in compressible flows can be described with the empirical expression proposed by Billig [26]:

$$x = R + \Delta - R_c cotan^2\theta \left[\left(1 + \frac{z^2 \tan^2 \theta}{R_c^2} \right)^{1/2} - 1 \right] \quad (1)$$

where R is the radius of the sphere, R_c is the vertex radius of curvature, and Δ is the standoff distance given by the empirical relation proposed by Ambrosio and Wortman [27]. The vertex radius is calculated by the following equation:

$$R_c/R = 1.143 \exp\left[0.54/(M-1)^{1.2}\right] \quad (2)$$

and the empirical standoff distance is calculated by the following equation:

$$\Delta/R = 0.143 \exp\left(3.24/M^2\right) \quad (3)$$

These equations have been established in a continuous regime and depend on the Mach number and the radius of the sphere, but do not include the degree of rarefaction of the flow. However, these equations are used to calculate the coordinates of the shock shapes applied for the simulation of debris interactions at very high altitudes. To this end, some authors have made analytical modifications but still without taking into account the pressure effects [28], [15].

In transitional regime, Vashchenkov, Kashovsky and Ivanov [29] are the only ones to propose a numerical study centered on the interaction between cylinders placed in the impact zone generated by a primary cylinder. The numerical approach is based on DSMC simulations. Their study shows on one hand, the presence of gradients gas dynamic parameters in the vicinity of the shock wave and on the other hand, that an insignificant change in the position of the fragment on each side of the shock implies a substantial change in the aerodynamic characteristics. This confirms the need to build an analytical description of shock waves in the transition and the slip regimes, based on experimental validations.

2.4. Determination of shock wave shapes

For lower pressure conditions (2.66 Pa and 7.99 Pa), shock wake shapes were analyzed using the glow discharge technique. For each case, two series of 200

raw images of the flow with and without spheres were recorded. The image that were used for the analysis results from the average of the images with the sphere minus the average of the images of the free stream. This processing improves the contrast of the image as shown in Fig. 5. The 'Canny-Edge-Detection' image processing method was used to detect the shock wave using the Matlab software. This is a commonly used method for first-order 'edge' detection, in which the 'edge' represents discontinuous changes in brightness in digital images [30].

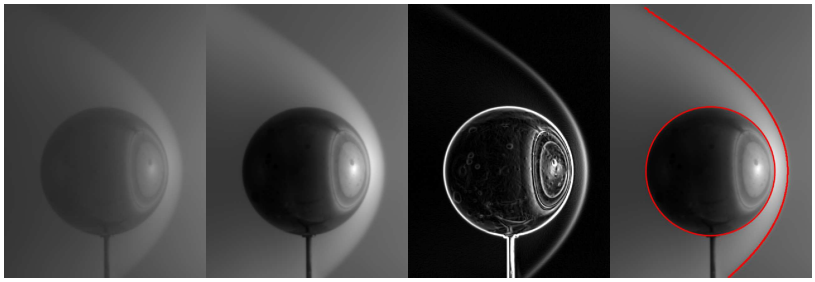

Figure 5: Images of the flow field around a 30 mm-sphere (Mach 4 – 7.99 Pa) from left to right: average field of the raw images, average field with background subtraction, gradient calculation, and edge detection function applied.

Fig. 5 illustrates the method obtained with a 30 mm diameter sphere in a flow at Mach 4 and 7.99 Pa. The standoff distance is then determined as the distance between the surface of the sphere and the shock wave on the stagnation line. Fig. 6(right) compares the shock waves obtained at 2.66 Pa and 7.99 Pa, where it is clear that the detachement increases as the pressure of the flow decreases, in other words as the Knudsen number increases. Fig. 6(left) presents the post-treatment shock waves compared with the shock wave described by Billig's equation. As observed, the rarefaction effects results in the deviation of the position of the shock from that predicted by Billig's empirical relationship.

For the highest pressure experimental condition at Mach 4 and 71 Pa, the visualization of the flow field around the sphere with the glow discharge tech-

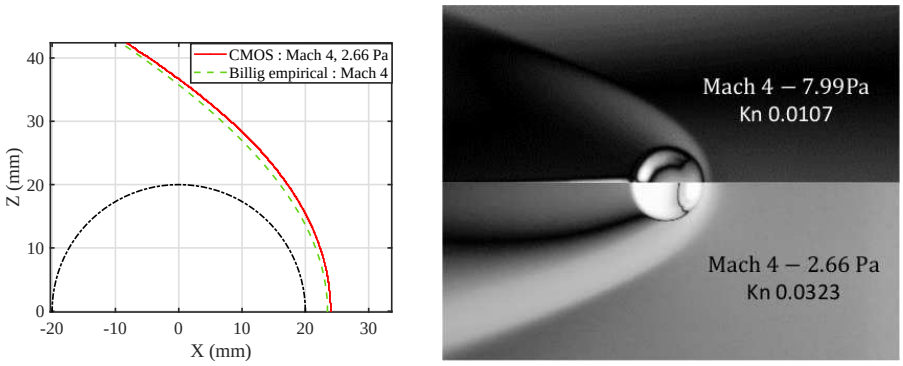

Figure 6: Shock wave positions: comparison of the experimental shock wave position obtained at Mach 4 – 2.66 Pa with the position given by the empirical relation of Billig (Eq. 1) around a 40 mm-diameter sphere (left panel), and comparison of the standoff distance obtained with a 5 mm-diameter sphere in a Mach 4 – 7.99 Pa flow (top) and in a Mach 4 – 2.66 Pa flow (bottom).

nique cannot be used because of the high background pressure, [17]. For this operating condition, the shape of the shock wave around spheres were detected from the total pressure profiles measured by the Pitot probe. For each diameter of the sphere, several vertical profiles (i.e., along z-axis) were performed at different longitudinal positions (i.e., along x-axis). The shock position is then determined from the analysis of Pitot pressure profiles. In viscous supersonic flow, the thickness of the boundary layer can be described as the distance along the axis of symmetry between the stagnation point of the model and the point of inflection of the density profile in the diffuse shock. In addition, the thickness of the shock layer increases with the degree of rarefaction [31]. On the stagnation pressure profile, the shock layer thickness is defined by pressures ranged between the free stream and the maximum value pressures (see Fig. 7). The position of the shock is located in this zone and is determined by the z coordinate of the minimum of the pressure gradient. The coordinate system is chosen so that the center of the spheres is at $x = 0, y = 0, z = 0$ mm.

The validation of the two shock characterization methods was carried out for a more rarefied case with the 10 mm sphere in the Mach 4 flow at 2.66 Pa. The

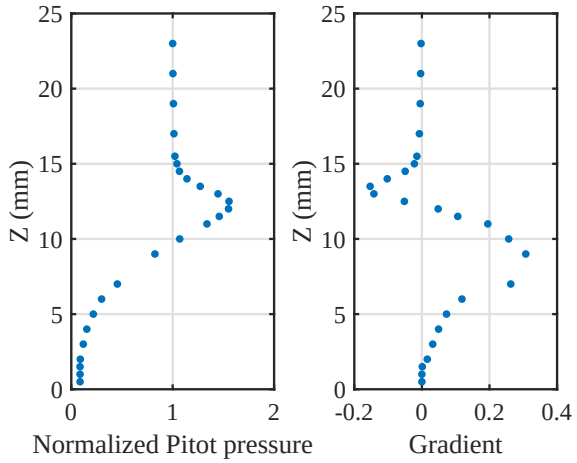

Figure 7: Shock detection from the pressure gradient. Sphere $R = 5$ mm in Mach $4 - 2.66$ Pa. Pressure profile at $x = -5$ mm (left). Pressure gradient profile (rigth).

Fig. 8 show the curve of shock wave determined from CMOS camera images and the positions of the shock calculated from vertical pitot profiles made for $x = -5$ mm, 0 mm and 2 mm. A good agreement is observed between the two methods, and this validates the Pitot probe method in low pressure conditions to determine the position of the shock around the spheres [25]. This method was applied to experimental cases at 71 Pa, where the glow discharge method is not applicable. Although, the Pitot method has limits because it does not allow exploring the flow in front of the sphere to determine the standoff distance of the shock.

The values of the Knudsen number for the experimental condition Mach 4-71 Pa are at the limit of continuous operation according to the usual definitions. In this case the empirical formulation of Billig (Eq. 1) could describe the shock wave coordinates as shown in Fig. 9 which compares the position of the shock wave obtained with the Pitot profile with the position of the shock given by the Billig equation for the 40 mm diameter sphere. From this result, we will assume that the experimental shape of the shock wave obtained with a flow at Mach 4 - 71 Pa can be described with empirical Billig equation [26], irrespective of the

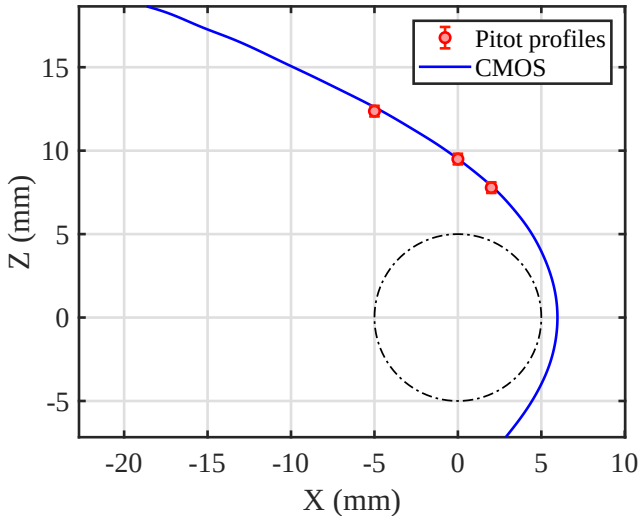

Figure 8: Comparison of shock analysis methods. Sphere R=5 mm Mach 4 – 2.66 Pa flow.

diameter of the sphere. The empirical equation used to calculate the Δ/R ratio (Eq. 3) then allows to estimate the standoff distance of the shock for the flow condition Mach 4 - 71 Pa for any sphere diameters. Hence, it can be expected that for smaller diameter spheres, Billig's approximation is not quite valid.

2.5. Comparison of experimental results and DS2V simulation

Despite various gas-surface interaction models that have been developed, the interactions are still not well understood for rarefied hypersonic conditions. The hypothesis of complete accommodation of the gas surface, which is valid in continuum regime, is no longer valid in rarefied conditions. However, these interactions govern the transfer of momentum and energy from the gas to the solid surface and will therefore directly influence the aerodynamic forces on the surface [32].

The Monte-Carlo calculation program DS2V, developed by Bird, [33] [34] was used to simulate the test case Mach 4 – 7.99 Pa and the 40 mm diameter sphere. Three numerical simulations were carried out with different accommodation coefficients, and the results were then compared with the experimental ones.

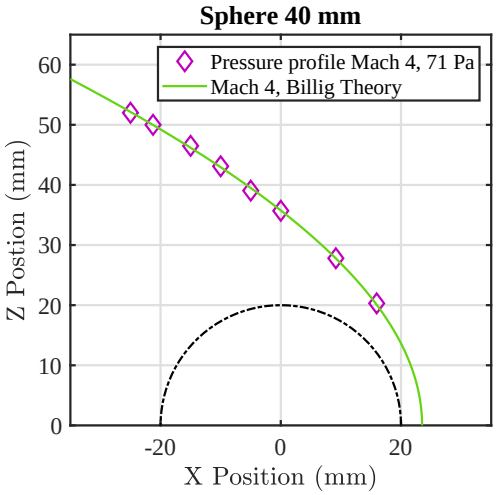

Figure 9: Shock wave position around the 40 mm-diameter sphere for the Mach 4 – 71 Pa flow condition. Data points correspond to the shock wave position estimated from the Pitot profiles.

The free stream conditions are those presented on Tab 2.

The values of accommodation coefficients range between 0 and 1, defining the specular and the diffusive, fully accommodated re-emissions, respectively. The DS2V code implements the Maxwell and the Cercignani-Lampis model (CLL). The diffusive, fully accommodated Maxwell model is the default option, whatever the gas-surface interaction can be changed by inputting the fraction (f) of molecules re-emitted specularly [35]. In the present work, simulations were achieved with CLL model and with normal accomodation parameters $a_n = 0.9$, 0.8 and 0.7.

Fig. 10 presents the total pressure profile for $x = 0$ mm, calculated with DS2V for $a_n = 0.9$, 0.8 and 0.7, where significant differences are observed, especially with regard to the position of the shock. A good agreement is found for the DS2V simulation with $a_n = 0.9$ compared to the experimental results as presented in Fig. 11 for different axial positions around the sphere $x = -5$, 0 and 8 mm. Fig. 12 presents the comparison of the DS2V calculated pressure flow field with the experimental CMOS camera flow field. As observed the

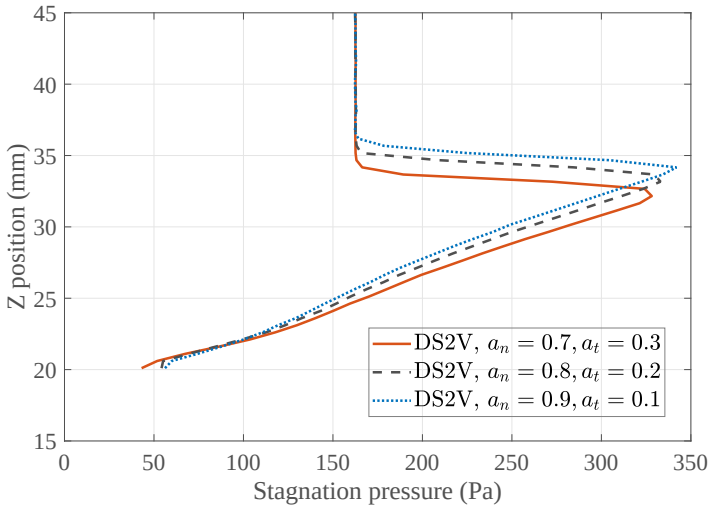

Figure 10: Effect of accommodation coefficients in pressure profiles at $x = 0$ mm calculated with DS2V simulation code. Mach 4 – 7.99 Pa, 40 mm sphere diameter.

295 experimental and numerical shock shapes fits well presenting a good agreement of the standoff distance.

2.6. Analysis of the standoff distance behavior

In the case of the Mach 4 – 2.66 Pa and Mach 4 – 7.99 Pa flow conditions, shock wave standoff distances were determined from the analysis of the CMOS 300 camera images using the glow discharge technique (Fig. 5). The operating conditions correspond to the slip flow regime with $Kn_D > 2 \times 10^{-3}$. For the Mach 4 – 71 Pa flow condition, the empirical equation of Ambrosio and Wortman (Eq. 3) was used to calculate the value of shock wave standoff distance. Fig. 13 shows the standoff distances according to the radius of the sphere for the three 305 experimental flow conditions. One can observe that three different sets of data points are clearly distinct, meaning that the empirical equation of Ambrosio and Wortman [27] fails to evaluate accurately the standoff distance in the case of flow conditions typical of the slip flow regime, and will probably fail for flow regimes nearest the free molecular regime. In addition, Fig. 13 shows that the

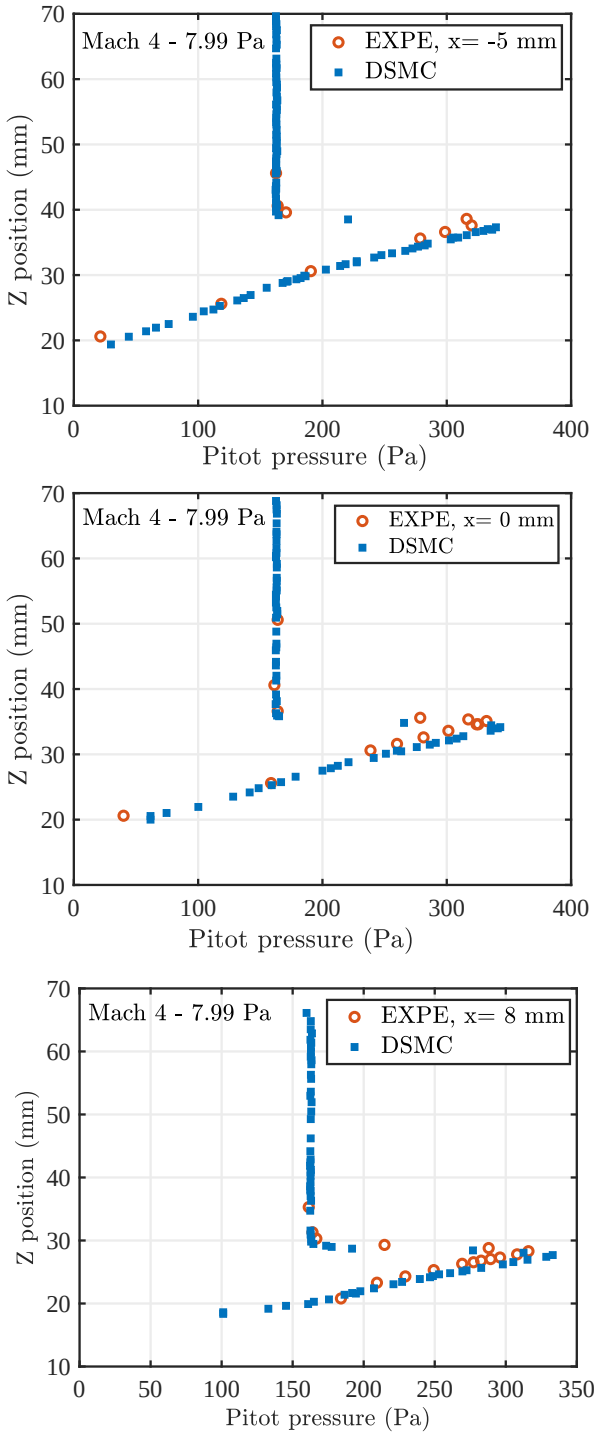

Figure 11: Comparison between experimental pressure profiles with DS2V calculated pressures for $x = -5$, 0 and 8 mm.

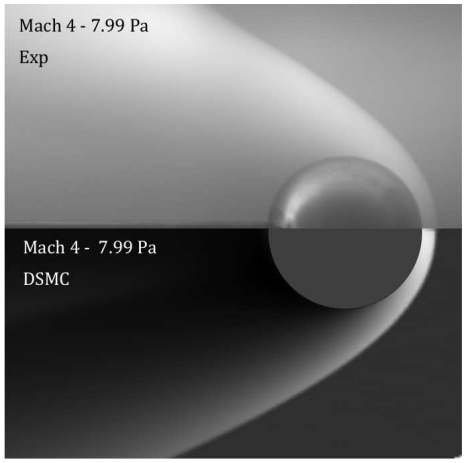

Figure 12: Comparison of the experimental and DS2V flow fields obtained at Mach 4 – 7.99 Pa with a 40 mm diameter sphere.

standoff distance increases linearly with the radius of the sphere, irrespective of the rarefaction level of the flow (for the slip flow regime).

The rarefaction level can be represented by the Knudsen number Kn, which was calculated for each experimental conditions with respect to the diameter of the sphere (Fig. 2) and the flow conditions of the present study (Tab. 1-3). Fig. 14 shows the variation of the Δ/R ratio as a function of the Knudsen number Kn_D (based on the sphere diameter).

One can observe a sharp increase of the values Δ/R when the Knudsen number becomes greater than 6×10^{-3}, thus showing that the standoff distance predicted by the Billig's equation are largely under estimated when the flow obeys the slip regime. Indeed, as presented in Fig. 15, the deviation between the experimental standoff and the one predicted by the Billig's equation can reach 70 % for a Knudsen number of 0.03. The deviation range are still between 10 and 20 % for Knudsen values, which according to the theory, corresponds to the continuous regime. It is important to note that the range of the Knudsen number values, according the experimental test cases presented in this work, correspond to the beginning of slip regime, which suggest that this discrepancy should grow when approaching the free molecular regime, before reaching a

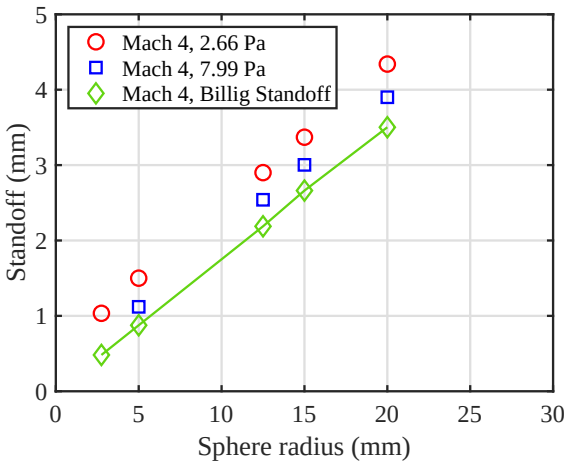

Figure 13: Standoff distance according to the sphere radius for the 3 freestream pressures tested at Mach 4. Data point for the 71 Pa case correspond to the values estimated with Eq. 3.

threshold value. These effects could modify the pressure distribution around the spheres, thus modifying the shape of the shock and the aerodynamic coefficients.

3. Conclusions

This experimental study aims to understand the influence of rarefaction effects on the re-entry trajectories of space debris better. This paper presents an experimental study focusing on the effects of rarefaction on the properties of the shock wave around the spheres. Experiments were carried out with the rarefied MARHy super/hypersonic wind tunnel, successively equipped with three different nozzles generating Mach 4 flows with static pressures of 71 Pa, 7.99 Pa and 2.66 Pa. Different diameters of spheres were chosen to obtain a wide range of Knudsen numbers corresponding to the slip regime. For each experimental condition shock shapes as well as the standoff distance of the shock were determined. Results show that the standoff distance increases with the Knudsen number, contradicting the formulation of Ambrosio and Wortman [27] beyond the continuous regime. The flow field around a 40 mm diameter sphere with a

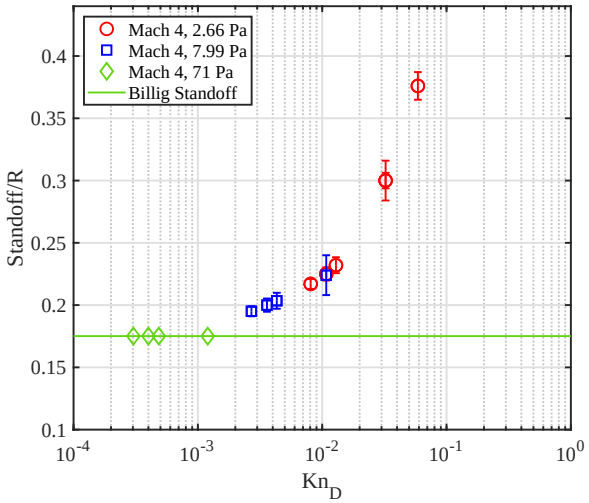

Figure 14: Ratio of the standoff distance with the sphere radius according to the Knudsen number.

Mach $4-7.99$ Pa condition was simulated with the DS2V code developed by G. Bird. The accommodation coefficients were adjusted to fit the experimental and numerical results. This study will be followed by drag coefficients measurements for spheres under similar experimental conditions, as the accommodation coefficients have repercussions on the aerodynamic drag coefficients. The objective is to establish an analytical formulation linking the standoff distances, the drag coefficients and the Knudsen number .

Acknowledgements

Nicolas Rembaut's Ph.D. fellowship is funded by the Région Centre-Val de Loire. This work was supported by the French National Research Agency (ANR) as part of the "Investments d'Avenir" Programme (LabEx CAPRYSSES; ANR-11-LABX-0006-01).

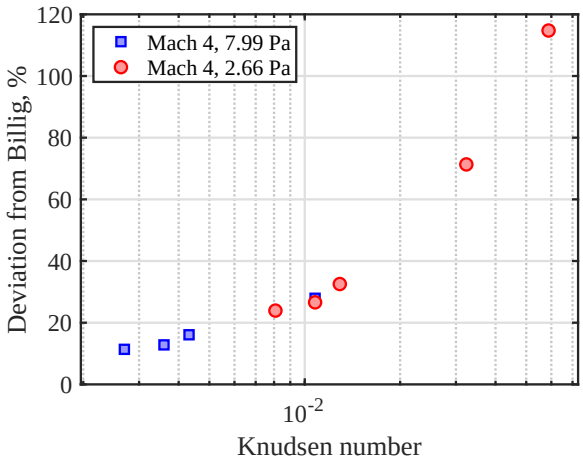

Figure 15: Relative difference between the experimental standoff distance and the value calculated with the empirical equation (Eq. 3) according to the Knudsen number.

References

[1] C. Bonnal, D. McKnight, C. Phipps, C. Dupont, S. Missonnier, L. Lequette, M. Merle, S. Rommelaere, Just in time collision avoidance–a review, Acta Astronautica 170 (2020) 637–651.

[2] H. Klinkrad, Space debris, Encyclopedia of Aerospace Engineering.

[3] J. J. Marichalar, C. L. Ostrom, Estimating drag and heating coefficients for hollow reentry objects in transitional flow using dsmc.

[4] I. P. Fuentes, D. Bonetti, F. Letterio, G. V. de Miguel, G. B. Arnao, P. Palomo, C. Parigini, S. Lemmens, T. Lips, R. Kanzler, Upgrade of esa's debris risk assessment and mitigation analysis (drama) tool: spacecraft entry survival analysis module, Acta Astronautica 158 (2019) 148–160.

[5] J. Annaloro, S. Galera, C. Thiebaut, M. Spel, P. Van Hauwaert, G. Grossir, S. Paris, O. Chazot, P. Omaly, Aerothermodynamics modelling of complex shapes in the debrisk atmospheric reentry tool: Methodology and validation, Acta Astronautica.

[6] G. Koppenwallner, B. Fritsche, T. Lips, H. Klinkrad, Scarab-a multi-disciplinary code for destruction analysis of space-craft during re-entry, in: Fifth European Symposium on Aerothermodynamics for Space Vehicles, Vol. 563, 2005, p. 281.

[7] Y. Prevereaud, J.-l. Vérant, J. Moschetta, F. Sourgen, M. Blanchard, Debris aerodynamic interactions during uncontrolled atmospheric reentry, in: AIAA Atmospheric Flight Mechanics Conference, 2012, p. 4582.

[8] A. Falchi, V. Renato, E. Minisci, M. Vasile, Fostrad: An advanced open source tool for re-entry analysis, in: 15th Reinventing Space Conference, 2017.

[9] G. Benedetti, N. Viola, E. Minisci, A. Falchi, M. Vasile, Low-fidelity modelling for aerodynamic characteristics of re-entry objects, in: Stardust Final Conference, Springer, 2018, pp. 247–264.

[10] W. Ziniu, H. Ruifeng, Q. Xi, W. Xiang, W. Zhe, Space debris reentry analysis methods and tools, Chinese Journal of Aeronautics 24 (4) (2011) 387–395.

[11] K. Moe, M. M. Moe, Gas–surface interactions and satellite drag coefficients, Planetary and Space Science 53 (8) (2005) 793–801.

[12] D. Dirkx, E. Mooij, Continuous aerodynamic modelling of entry shapes, in: AIAA Atmospheric Flight Mechanics Conference, 2011, p. 6575.

[13] P. A. Chambre, S. A. Schaaf, Flow of rarefied gases, Princeton University Press, 2017.

[14] L. Morsa, G. Zuppardi, A. Schettino, R. Votta, Analysis of bridging formulae in transitional regime, in: AIP Conference Proceedings, Vol. 1333, American Institute of Physics, 2011, pp. 1319–1324.

[15] Y. Prevereaud, Contribution à la modélisation de la rentrée atmosphérique des débris spatiaux, Ph.D. thesis (2014).

[16] S. J. Laurence, N. J. Parziale, R. Deiterding, Dynamical separation of spherical bodies in supersonic flow, Journal of Fluid Mechanics 713 159–182. doi:10.1017/jfm.2012.453.

[17] S. Coumar, V. Lago, Influence of mach number and static pressure on plasma flow control of supersonic and rarefied flows around a sharp flat plate, Experiments in Fluids 58 (6) (2017) 74.

[18] J. Allegre, The SR3 low density wind tunnel - facility capabilities and researchdevelopment, in: 28th Joint Propulsion Conference and Exhibit, American Institute of Aeronautics and Astronautics. doi:10.2514/6.1992-3972.

[19] S. Coumar, Study of physical mechanisms induced by a plasma actuator for super/hypersonic rarefied flows applied to atmospheric entries, Ph.D. thesis (2017).

[20] S. Chue, Pressure probes for fluid measurement, Progress in aerospace sciences 16 (2) (1975) 147–223.

[21] J. Allegre, M. Cabaret, M. Raffin, Low-pressure measurement by thermistor, and orifice-effect determination in rarefied gas flows, NASA STI/Recon Technical Report N (Sep. 1974).

[22] A. K. Mohamed, T. Pot, B. Chanetz, Diagnostics by electron beam fluorescence in hypersonics, in: ICIASF'95 Record. International Congress on Instrumentation in Aerospace Simulation Facilities, IEEE, 1995, pp. 14–1.

[23] S. Fisher, D. Bharathan, Glow-discharge flow visualization in low-density free jets, Journal of Spacecraft and Rockets 10 (10) (1973) 658–662.

[24] V. Kalugin, Glow discharge measurement of gas density in supersonic rarefied flow, Journal of Applied Mechanics and Technical Physics 10 (2) (1969) 277–281.

[25] E. Menier, Influence d'une décharge électrique continue sur un écoulement supersonique raréfié, Ph.D. thesis, Orléans (2007).

[26] F. S. Billig, Shock-wave shapes around spherical-and cylindrical-nosed bodies., Journal of Spacecraft and Rockets 4 (6) 822–823. doi:10.2514/3.28969.

[27] A. Ambrosio, A. Wortman, Stagnation-point shock-detachment distance for flow around spheres and cylinders in air, Journal of the Aerospace Sciences 29 (7) 875–875. doi:10.2514/8.9622.

[28] S. J. Laurence, R. Deiterding, G. Hornung, Proximal bodies in hypersonic flow, Journal of Fluid Mechanics 590. doi:10.1017/S0022112007007987.

[29] P. Vashchenkov, A. Kashkovsky, M. Ivanov, Aerodynamics of fragment in spacecraft wake, in: AIP Conference Proceedings, Vol. 663, American Institute of Physics, 2003, pp. 226–233.

[30] T. R. Fujimoto, T. Kawasaki, K. Kitamura, Canny-edge-detection/rankine-hugoniot-conditions unified shock sensor for inviscid and viscous flows, Journal of Computational Physics 396 (2019) 264–279.

[31] N. Isakova, A. Kraiko, Shock-layer thickness for supersonic viscous gas flow past blunt bodies, Fluid Dynamics 4 (6) (1969) 95–98.

[32] J. Padilla, I. Boyd, Assessment of gas-surface interaction models in dsmc analysis of rarefied hypersonic flow, in: 39th AIAA Thermophysics Conference, 2007, p. 3891.

[33] G. Bird, The ds2v/3v program suite for dsmc calculations, in: AIP conference proceedings, Vol. 762, American Institute of Physics, 2005, pp. 541–546.

[34] G. Bird, Forty years of dsmc, and now?, in: AIP Conference Proceedings, Vol. 585, American Institute of Physics, 2001, pp. 372–380.

[35] G. Zuppardi, Influence of partial accommodation coefficients on the aerodynamic parameters of an airfoil in hypersonic, rarefied flow, Advances in aircraft and spacecraft science 2 (4) (2015) 427.